



## OPEN ACCESS

## EDITED BY

Salam Dhou,  
American University of Sharjah, United  
Arab Emirates

## REVIEWED BY

Silambarasan Anbumani,  
The University of Arkansas for Medical  
Science, United States  
Bashar Al-Qaisieh,  
Leeds Teaching Hospitals NHS Trust  
Research and Innovation Department,  
United Kingdom

## \*CORRESPONDENCE

Jessica Prunaretty  
✉ Jessica.prunaretty@icm.unicancer.fr

RECEIVED 28 November 2025

REVISED 13 January 2026

ACCEPTED 02 February 2026

PUBLISHED 20 February 2026

## CITATION

Prunaretty J, Colombo L, Romdhani S,  
Teboul O, Azria D, Paragios N and  
Fenoglio P (2026) Self-learning  
GAN based synthetic CT generation:  
unlocking CBCT-based  
adaptive radiotherapy.  
*Front. Oncol.* 16:1756153.  
doi: 10.3389/fonc.2026.1756153

## COPYRIGHT

© 2026 Prunaretty, Colombo, Romdhani,  
Teboul, Azria, Paragios and Fenoglio.  
This is an open-access article distributed  
under the terms of the [Creative  
Commons Attribution License \(CC BY\)](https://creativecommons.org/licenses/by/4.0/).  
The use, distribution or reproduction in  
other forums is permitted, provided the  
original author(s) and the copyright  
owner(s) are credited and that the  
original publication in this journal is  
cited, in accordance with accepted  
academic practice. No use, distribution  
or reproduction is permitted which does  
not comply with these terms.

# Self-learning GAN based synthetic CT generation: unlocking CBCT-based adaptive radiotherapy

Jessica Prunaretty<sup>1\*</sup>, Lorenzo Colombo<sup>2</sup>, Sami Romdhani<sup>3</sup>,  
Olivier Teboul<sup>3</sup>, David Azria<sup>1</sup>, Nikolaos Paragios<sup>3,4</sup>  
and Pascal Fenoglio<sup>1</sup>

<sup>1</sup>Department of Radiation Oncology, Institut du Cancer de Montpellier, Montpellier, France, <sup>2</sup>Clinical affairs, TheraPanacea, Paris, France, <sup>3</sup>AI Engineering, TheraPanacea, Paris, France, <sup>4</sup>Chief Executive Officer (CEO), TheraPanacea, Paris, France

**Purpose/objectives:** This study proposes and clinically evaluates synthetic CT (sCT) images generated from multi-center CBCT scans using artificial intelligence, with the aim of fully leveraging CBCT for adaptive radiotherapy in patients with pelvic, head-and-neck, lung, and breast cancer.

**Materials and methods:** In collaboration with TheraPanacea (Paris, France), AI-based sCT models were developed for multiple anatomical sites using a cycleGAN architecture. The study included 51 patients from two European institutions diagnosed with head-and-neck, lung, pelvic or breast cancer and treated with CBCT-based position verification. CBCT scans were acquired using two linear accelerator systems (Varian and Elekta). Image accuracy was assessed using MAE, SSIM, and PSNR. For dosimetric evaluation, planning CTs (pCTs) were non-rigidly registered to CBCTs. Treatment plans were created on the pCT using a clinical TPS to meet standard clinical criteria, then recalculated on both the warped CT (wCT) and sCT. Dose distributions were compared using global gamma passing rates and dose-volume metrics.

**Results:** The proposed model substantially improved image quality compared with CBCT. MAE decreased from  $122.95 \pm 50.07$  to  $23.65 \pm 10.09$ , while SSIM increased from  $0.78 \pm 0.12$  to  $0.97 \pm 0.03$  and PSNR from  $35.01 \pm 7.24$  to  $44.35 \pm 7.07$ . Dose-metric comparisons showed strong agreement between the pCT and wCT, with median relative differences within 0.5% for both targets and organs at risk. Median gamma passing rates for 2%/2 mm and 3%/3 mm criteria (10% threshold) reached 100% across all anatomical sites. No performance differences were observed between Elekta- and Varian-sCTs.

**Conclusion:** This multi-center study demonstrates the feasibility of generating clinically acceptable AI-based sCTs from CBCT for multiple anatomical sites, yielding consistent image quality improvements and reliable dosimetric accuracy.

## KEYWORDS

adaptive radiotherapy, artificial intelligence, CBCT, deep learning, synthetic CT

# 1 Introduction

Online adaptive radiotherapy (oART) is becoming more widely used in clinical practice worldwide due to its ability to re-optimize treatment plans to account for daily patient-specific treatment variations (1, 2). The first clinical workflow programs for online ART were established using magnetic resonance guided radiotherapy (MRgRT) (3, 4) and Ethos<sup>®</sup> Therapy was the first oART solution commercialized by Varian Medical System using cone beam computed tomography (CBCT) images (5).

The use of CBCT for dose calculation holds significant appeal when it comes to dose reporting and monitoring, particularly in the context of dose-guided adaptive radiotherapy. Although CBCT has revolutionized image-guided radiotherapy (IGRT) and is extensively used for daily patient setup (6), its use for plan adaptation is still limited. The main reasons are the artefacts related with scatter and the reconstruction algorithms, which reduce image quality and CBCT-based dose calculation accuracy (7–9). Several solutions have been proposed using deformable image registration (10–12), scatter correction (13, 14), or rescaling of Hounsfield unit intensities (15).

With the development of artificial intelligence, studies have focused on deep learning approaches (16–19). Kia et al. (20) was the first team to create a so-called synthetic-CT from a CBCT. They developed a deep convolutional neural network method for improving CBCT image quality for prostate cancer patients. Since then, the number of investigations have grown, resulting in many different architectures. In the recent years, the generative adversarial network (GAN) is one of the most developed architectures due to the anatomical preservation and the use of unpaired data sets. Xue et al. (21) generated sCT from head and neck CBCT using the CycleGAN, Pix2Pix and U-Net models and the performance of CycleGAN was proved to be best among three models in terms of image quality and dose accuracy. Likewise, Pang et al. (22) compared four deep learning architectures (cycleGAN, Unet, Unet + cycleGAN, conditional GAN) for generating nasopharynx CBCT and showed the superiority of the conditional GAN model in an adaptive proton treatment planning application. Maspero et al. (23) also demonstrated the feasibility to use a single cycle-GAN architecture for different anatomical sites. However, few studies investigated the model training using multi-center datasets (24) as proposed for MR-to-CT synthesis (25, 26). This study introduces and evaluates an artificial intelligence-based method for synthetic CT (sCT) generation in a pre-clinical validation setting to address these challenges, with the aim of fully harnessing the potential of CBCT for adaptive radiotherapy in patients with pelvic, head and neck, lung, and breast cancers.

## 2 Materials and methods

### 2.1 Deep learning workflow

Cycle generative adversarial networks (CycleGANs) are deep learning architectures designed to learn bijective transformations

between image modalities. Training a model to generate CT images from CBCTs is challenging due to the intrinsic difficulty of acquiring perfectly aligned CBCT–CT pairs. To overcome this limitation, a two-stage cycle architecture combined with a patented CBCT simulation approach, was developed.

In the first stage, perfectly aligned CBCT–CT pairs were generated by simulating CBCT acquisitions directly from real CT volumes. This simulation reproduces the physical principles of clinical CBCT imaging, in which image quality degradation primarily arises from the limited number of projections compared to conventional CT. Specifically, simulated CBCTs were obtained by projecting a reduced number of cone-beam projections from CT volumes onto integral planes, followed by 3D reconstruction using an inverse Radon transform based on the method described by Biguri et al. (27). By construction, these simulated CBCTs are fully aligned with their corresponding CTs, thereby eliminating registration inaccuracies and enabling robust supervised training.

In the second stage, the model was refined using real CBCT data, allowing the network to adapt to clinical image characteristics while preserving spatial consistency. The GAN was thus trained to generate synthetic CTs from real CBCTs that became indistinguishable from true CT images. This two-stage strategy, combining physics-based CBCT simulation with cycle-consistent adversarial learning, distinguishes our approach from previously reported models that rely on imperfectly registered CBCT–CT datasets or purely unsupervised training.

The training and validation dataset comprised 1063 planning CTs and 228 CBCTs for head and neck, 278 planning CTs and 174 CBCTs for breast, 484 planning CTs and 324 CBCTs for thorax, and 317 planning CTs with 194 CBCTs for pelvis. Data were provided by three European institutions (referred to as Centers A, B and C) and were split into training (80%) and validation (20%) sets. Details of simulated CBCTs derived from planning CTs, stratified by anatomy, center, and CBCT vendor, as well as imaging protocols, are reported in [Supplementary Material 1](#).

### 2.2 Augmentation of the synthetic CT

As the CBCT field of view (FOV) is smaller than that of the planning CT, the synthetic CT (sCT) is extended using information from the planning CT to enable organ-at-risk segmentation and dose computation. The augmentation is performed in the X, Y, and Z directions, with particular emphasis on the superior–inferior axis. First, the CBCT FOV and the external contours of both the sCT and the planning CT are detected. A deformable registration is then computed between the planning CT and the sCT. From this registration, a variable-weight mask is generated, assigning a weight of 1 inside the sCT external contour and an exponentially decreasing weight outside the contour. The deformable displacement field is resampled using this mask, resulting in a hybrid transformation: near the sCT FOV, the deformation corresponds to the deformable registration, ensuring geometric continuity, while far from the sCT FOV the deformation progressively vanishes, effectively reverting to a rigid transformation and thus minimizing assumptions on patient geometry.

The planning CT and its contours are warped using this resampled displacement field, followed by a rigid registration between the sCT and the warped planning CT (wCT). Finally, the superior and inferior boundary slices of the sCT are identified, and slices from the wCT are appended above and below these boundaries to obtain an augmented synthetic CT with a full planning CT FOV and without geometric discontinuities.

## 2.3 Patient selection

An independent, retrospective cohort of 10 prostate, 16 head and neck, 12 lung and 13 breast cancer patients treated at two leading European cancer treatment centers (referred to as Centers B and D) was selected for this evaluation. These testing datasets were entirely different from the cycle-GAN model training datasets. CBCT scans were performed using equipment from two different linac manufacturers, Varian and Elekta. For each patient, a single CBCT fraction was randomly selected and used for sCT generation and comparison with the planning CT.

## 2.4 Image accuracy

Mean absolute error (MAE), structural similarity index measure (SSIM), peak signal to noise ratio (PSNR) were computed to assess the image accuracy. The MAE quantifies the average absolute pixel-wise difference between the sCT and the reference CT, defined as:

$$MAE = \frac{1}{N} \sum_{i=1}^N |x_i - y_i|$$

where  $x_i$  and  $y_i$  represent pixel intensities of the ground truth and synthetic images, respectively, and  $N$  is the total number of pixels. Lower MAE values indicate higher accuracy.

The SSIM assesses perceptual similarity by comparing luminance, contrast, and structural information between the two images, and is given by:

$$SSIM = \frac{(2\mu_x\mu_y + C_1)(2\sigma_{xy} + C_2)}{(\mu_x^2 + \mu_y^2 + C_1)(\sigma_x^2 + \sigma_y^2 + C_2)}$$

where  $\mu_x$ ,  $\mu_y$  are mean intensities,  $\sigma_x$ ,  $\sigma_y$  are standard deviations,  $\sigma_{xy}$  is the covariance, and  $C_1$ ,  $C_2$  are small constants to prevent division instability SSIM values range from 0 (no similarity) to 1 (perfect similarity).

The PSNR measures image fidelity relative to the maximum possible intensity value, expressed as:

$$PSNR = 20 \log_{10} \left( \frac{MAX_{pix}}{\sqrt{MSE}} \right)$$

where  $MAX_{pix}$  is the maximum pixel intensity and MSE is the mean squared error. Overall, lower MAE and higher SSIM and PSNR values indicate closer correspondence and improved agreement between the sCT and the reference CT.

To evaluate the Hounsfield Unit (HU) differences between sCT and CT images, the planning CT images were deformably registered to the corresponding CBCT images to generate reference CT datasets for testing. The synthetic CT images were subsequently compared with the CBCT images to assess the reconstruction

performance. All similarity metrics were computed within the CBCT-defined mask.

## 2.5 Dosimetric evaluation

Planning CTs were deformably registered to the CBCTs for each patient to account for changes in body anatomy and positioning. Treatment plans were optimized on the wCT and recalculated on the sCTs for the dosimetric evaluation. Dose calculations were performed using the AAA algorithm within Eclipse TPS (version 15.6, Varian Medical Systems, Palo Alto, CA, USA) in a volumetric modulated arc therapy (VMAT) configuration using a dose calculation grid size of 0.25 cm. Dose prescriptions were detailed in [Supplementary Material 1](#).

For analysis, wCT and sCT were compared using DVH parameters for PTV and organs at risk. Given the variations in dose prescriptions, the dose comparison was conducted using the relative dose difference, which is defined as:

$$\Delta D_x = \frac{D_x^{sCT} - D_x^{wCT}}{D_x^{wCT}}$$

With  $D_x^{sCT}$  the dose metric from the sCT and  $D_x^{wCT}$  the dose metric from the wCT. Reference structures for DVH parameters were rigidly transferred from the planning CT to sCT. In the case of simultaneous integrated boost treatment, the larger PTV was retained. Dose metrics are detailed in [Table 1](#). In addition, 3D dose distributions were evaluated using global gamma criteria (2%/2mm and 3%/3mm) with a 10% threshold using VeriSoft software (PTW Dosimetry, Freiburg, Germany). The 3%/3 mm and 2%/2 mm criteria were selected to enable comparison with the existing literature.

## 3 Results

Training of the synthetic CT model required approximately two weeks. The images were resampled to an isotropic resolution of 1 mm<sup>3</sup> and cropped or padded to a fixed size of 16 × 512 × 512 voxels (Z, Y, X). Model convergence was achieved after approximately 200 training epochs using NVIDIA RTX 3090 GPUs. Using two GPUs, the generation of a sCT image took about 30 seconds, with an additional 20 seconds for augmentation, resulting in a total generation time of roughly 50 seconds per case. Generation time may vary depending on hardware configuration and imaging parameters.

[Figure 1](#) presents representative examples of sCTs generated by the AI-based model, illustrating the comparison of Hounsfield Units with the corresponding deformably registered CT images for the male pelvis, thorax, head and neck, and breast regions. The image quality of sCTs was markedly improved compared with CBCT, primarily due to reduced scatter artifacts and smoother the HU distributions.

The [Table 2](#) summarizes the quantitative image similarity metrics for each anatomical site. Overall, the MAE decreased from 122.95 ± 50.07 to 23.65 ± 10.09, the SSIM increased from

TABLE 1 Dose metrics used for the dosimetric evaluation.

|             |             |                     |        |             |                     |
|-------------|-------------|---------------------|--------|-------------|---------------------|
| Prostate    | PTV         | D <sub>2%</sub>     | Thorax | PTV         | D <sub>2%</sub>     |
|             |             | D <sub>50%</sub>    |        |             | D <sub>50%</sub>    |
|             |             | D <sub>95%</sub>    |        |             | D <sub>95%</sub>    |
|             |             | D <sub>98%</sub>    |        |             | D <sub>98%</sub>    |
|             | Rectum      | D <sub>50%</sub>    |        | Spinal cord | D <sub>0.05cc</sub> |
|             |             | D <sub>25%</sub>    |        | Lung        | V <sub>20Gy</sub>   |
|             |             | D <sub>mean</sub>   |        |             | D <sub>mean</sub>   |
|             | Bladder     | D <sub>50%</sub>    |        | Heart       | V <sub>30Gy</sub>   |
|             |             | D <sub>25%</sub>    |        |             | D <sub>mean</sub>   |
|             |             | D <sub>mean</sub>   |        |             |                     |
| Head & Neck | PTV         | D <sub>2%</sub>     | Breast | PTV         | D <sub>2%</sub>     |
|             |             | D <sub>50%</sub>    |        |             | D <sub>50%</sub>    |
|             |             | D <sub>95%</sub>    |        |             | D <sub>95%</sub>    |
|             |             | D <sub>98%</sub>    |        |             | D <sub>98%</sub>    |
|             | Spinal cord | D <sub>0.05cc</sub> |        | Spinal cord | D <sub>0.05cc</sub> |
|             | Parotid     | D <sub>mean</sub>   |        | Lung        | V <sub>20Gy</sub>   |
|             | Brainstem   | D <sub>1cc</sub>    |        |             | D <sub>mean</sub>   |
|             | Larynx      | D <sub>mean</sub>   |        | Heart       | V <sub>30Gy</sub>   |
|             |             |                     |        |             |                     |

0.78 ± 0.12 to 0.97 ± 0.03 and the PSNR increased from 35.01 ± 7.24 to 44.35 ± 7.07 when comparing CBCT and sCT images. Despite variations in CBCT image quality between Varian and Elekta acquisitions, only minor differences were observed in the corresponding sCT reconstructions (Table 3).

Figure 2 shows the relative dose difference for the PTV and the organs at risk between plans calculated using the synthetic CT and the warped CT for pelvis, thorax, head and neck and breast localizations. The median relative dose differences for the PTV were lower than 0.5% for each dose metric (D<sub>98%</sub>, D<sub>95%</sub>, D<sub>50%</sub>, and D<sub>2%</sub>). The maximum reported value was 2.95% for D<sub>98%</sub>, equivalent to 1.05Gy for the thorax. Concerning the organs at risk, the median relative dose difference were less than 0.5%, regardless the dose metrics and localizations assessed. The maximal difference was -4.46% for V<sub>30Gy</sub> of the heart, corresponding to 0.10Gy. The largest relative dose difference for PTV and heart are from the same patient illustrated in Figure 3.

The median global gamma analysis using two tolerance criteria (3%/3 mm and 2%/2 mm) with a 10% dose threshold demonstrated strong agreement between the dose distributions calculated on the synthetic CT and the warped CT (Table 4). The lowest gamma passing rate was observed for the thorax case, with a value of 96.6% for the 2%/2 mm criterion. This corresponded to the same patient presented earlier (Figure 3).

## 4 Discussion

This study introduced 3D cycle GAN models for generating synthetic-CTs from CBCT images in cases of pelvic, head and neck,

lung, and breast cancer. The key strengths of this work include its multi-centric approach, incorporating CBCT images from various linac manufacturers with differing characteristics, and the extensive patient dataset used for model training, ensuring robust synthetic-CT generation. Additionally, the cycle GAN architecture's ability to function without paired images is particularly beneficial for areas like the pelvis, where anatomical variations are frequent.

Regarding the qualitative evaluation, the results obtained in this study are satisfying, showing a good agreement between the synthetic-CT and the warped CT. In addition, this research demonstrated that AI-driven synthetic CT generation from CBCT is clinically accurate across multiple anatomical sites. In terms of image accuracy, the MAE was 23, 65 ± 10, 09 for all confounded localizations. Dosimetric assessment showed median dose differences within 0.5% and median gamma pass rates of 100% for both the 3%/3mm and 2%/2mm criteria. Our results are consistent with recent literature that extends image quality analysis to include additional dose assessment (28–32). For example, O'Hara et al. (30) evaluated the image and dose accuracy of AI-guided sCTs generated from head and neck CBCT images. They reported a MAE of 79.4 HU, a gamma pass rate of 99.8% (2%/2mm, 20% dose threshold) and a generation time of 112 seconds. However, their dosimetric evaluation was limited to the CBCT field of view, which does not encompass the entire patient volume, potentially limiting its effectiveness in an adaptive workflow. Xie et al. (31) developed a technique similar to ours for handling truncated CBCTs in breast cancer cases and demonstrated excellent dose calculation accuracy with gamma pass rates of 98.98 ± 0.64% and 99.69 ± 0.22% for 2%/2mm and 3%/3mm criteria, respectively.

A primary limitation of this study is that the planning CT was used as the 'ground truth' to evaluate the quality of the sCTs

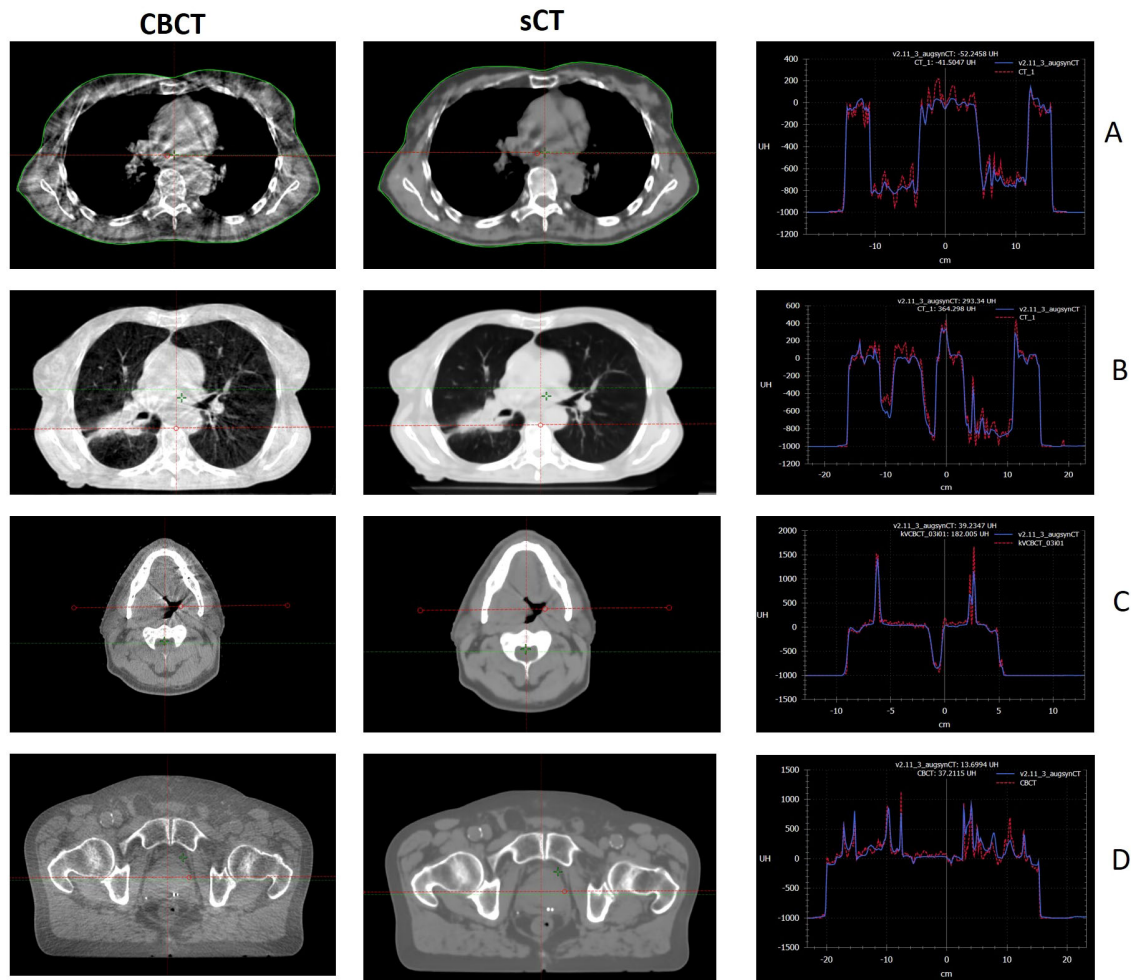


**FIGURE 1** Example of sCT (right) and the CBCT (left) images for breast (A), thorax (B), head and neck (C) and male pelvis (D) anatomies. Example of Hounsfield unit comparison between sCT (blue line) and CBCT (red line).

generated from CBCT data. Despite using a wrapped CT to reduce discrepancies, anatomical variations may still be introduced by the time interval between the planning CT and the CBCT acquisition, such as differences in organ filling, air cavity fluctuations, or tumour

regression, that can affect the agreement between the two image sets. Consequently, as illustrated in Figure 3, some of the observed deviations may be due to imperfections in the reference images rather than to limitations in the sCT generation process itself.

**TABLE 2** Comparison of MAE, SSIM and PSNR between CBCT and sCT images for breast, thorax, head and neck and male pelvis localizations.

| Anatomical site | Image type | MAE (HU)       | SSIM        | PSNR         |
|-----------------|------------|----------------|-------------|--------------|
| Breast          | CBCT       | 95.54 ± 23.30  | 0.79 ± 0.08 | 35.53 ± 5.51 |
|                 | sCT        | 25.99 ± 7.51   | 0.97 ± 0.03 | 43.54 ± 7.10 |
| Thorax          | CBCT       | 104.12 ± 31.03 | 0.73 ± 0.22 | 33.10 ± 9.64 |
|                 | sCT        | 32.74 ± 9.43   | 0.97 ± 0.02 | 43.12 ± 4.34 |
| Head&Neck       | CBCT       | 169.38 ± 58.13 | 0.81 ± 0.14 | 36.51 ± 6.95 |
|                 | sCT        | 15.11 ± 6.52   | 0.98 ± 0.02 | 47.75 ± 7.33 |
| Male pelvis     | CBCT       | 98.79 ± 36.24  | 0.74 ± 0.16 | 34.88 ± 6.21 |
|                 | sCT        | 23.39 ± 6.15   | 0.97 ± 0.03 | 41.44 ± 6.82 |
| Global          | CBCT       | 122.95 ± 50.07 | 0.78 ± 0.12 | 35.01 ± 7.24 |
|                 | sCT        | 23.65 ± 10.09  | 0.97 ± 0.03 | 44.35 ± 7.07 |

TABLE 3 Comparison of MAE, SSIM, and PSNR for CBCT and sCT images across different anatomical regions (breast, thorax, head and neck, and male pelvis).

| Image type | Breast       |        |      | Thorax |        |      | Head & neck |        |      | Male pelvis |        |      |       |
|------------|--------------|--------|------|--------|--------|------|-------------|--------|------|-------------|--------|------|-------|
|            | Manufacturer | MAE    | SSIM | PSNR   | MAE    | SSIM | PSNR        | MAE    | SSIM | PSNR        | MAE    | SSIM | PSNR  |
| CBCT       | Varian       | 78.60  | 0.81 | 36.05  | 96.32  | 0.72 | 30.97       | 103.93 | 0.87 | 40.94       | 67.01  | 0.81 | 36.66 |
|            | Elekta       | 115.30 | 0.78 | 34.92  | 121.24 | 0.83 | 39.65       | 208.65 | 0.77 | 33.85       | 130.56 | 0.67 | 33.10 |
| sCT        | Varian       | 20.96  | 0.98 | 46.03  | 32.51  | 0.96 | 39.65       | 13.47  | 0.99 | 50.48       | 22.03  | 0.97 | 41.56 |
|            | Elekta       | 31.86  | 0.95 | 40.63  | 32.90  | 0.98 | 45.60       | 16.09  | 0.98 | 46.11       | 24.76  | 0.96 | 41.32 |

Results are reported separately for images acquired with Varian and Elekta systems.

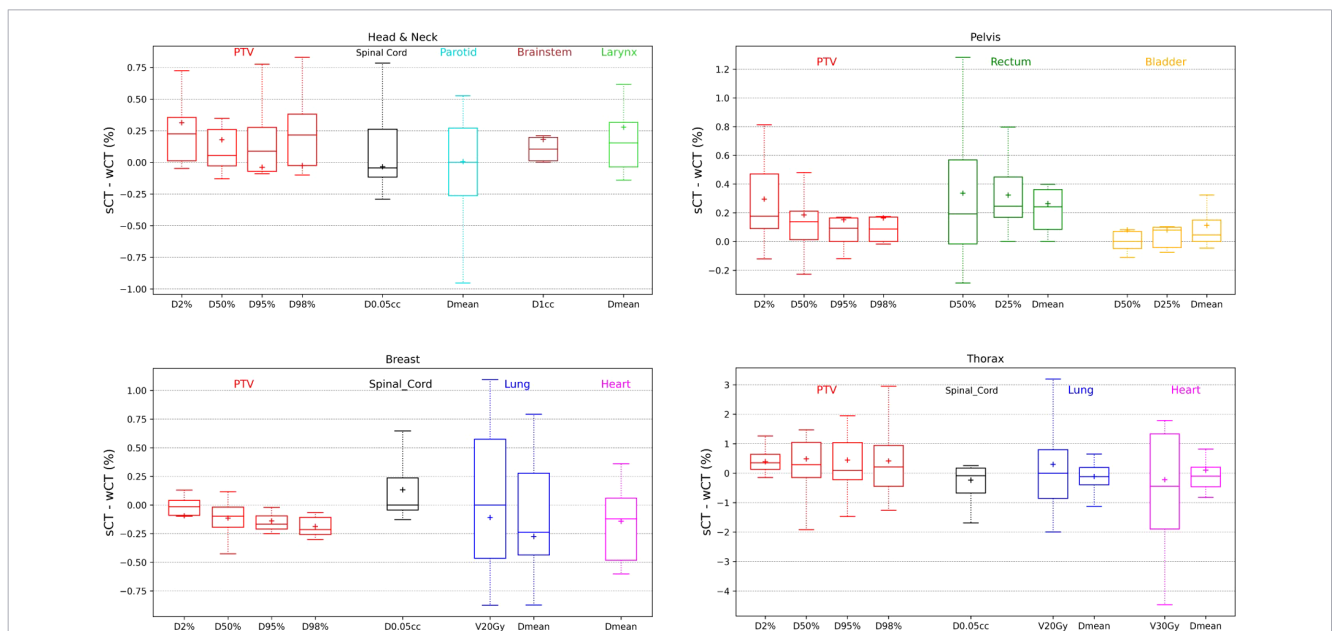


FIGURE 2 Relative dose deviations between the synthetic CT and the warped CT for the PTV and organs at risk using different dose metrics for male pelvis, thorax, head and neck and breast localizations.

Furthermore, although differences in CBCT image quality were observed between the Varian and Elekta systems, these did not appear to cause any noticeable deterioration in the corresponding sCTs. However, the relatively small number of test cases per anatomical site and per manufacturer reduces the strength and generalisability of these findings. Therefore, expanding the patient

cohort in future studies will be essential to improve the statistical robustness of the conclusions. Finally, the sCT generation framework was evaluated in a pre-clinical validation setting and was not clinically deployed at the time of the study. Consequently, the results reflect a controlled research environment and may not fully capture the constraints and variability encountered in routine

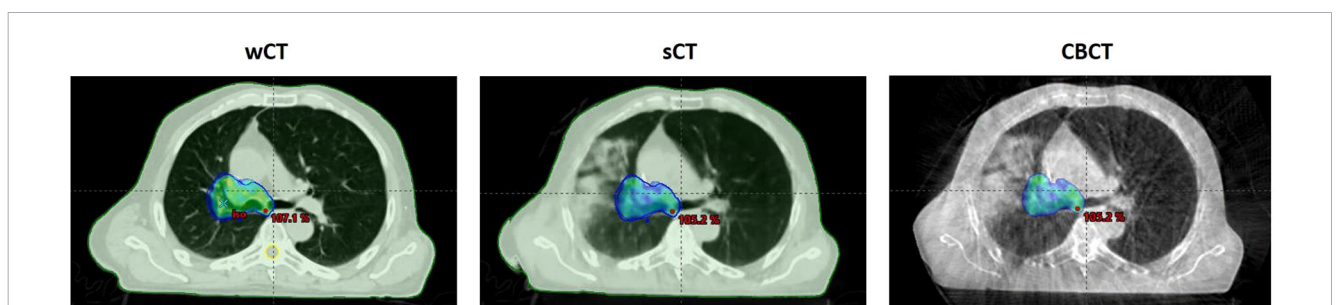


FIGURE 3 Example of comparison of dose distribution (95% isodose) calculated on the wCT (left), sCT (center) and displayed on the CBCT (right) for a patient treated for a lung cancer.

TABLE 4 Comparison of the global gamma passing rates for pelvis, thorax, head and neck and breast localizations using 3%3mm and 2%2mm criterion with 10% dose thresholds.

| Anatomical site | Gamma pass rates (Median [Min-Max]) |                  |
|-----------------|-------------------------------------|------------------|
|                 | 3%3mm                               | 2%2mm            |
| Pelvis          | 100 [99.6 - 100]                    | 100 [99.2 - 100] |
| Thorax          | 100 [99.7 - 100]                    | 100 [96.6 - 100] |
| Head & Neck     | 100 [98.7 - 100]                    | 100 [97.4 - 100] |
| Breast          | 100 [100]                           | 100 [99.9 - 100] |

clinical workflows. While deformable image registration between planning CT and CBCT is a mature and commercially available approach for adaptive radiotherapy (Ethos, Raysearch, RadFormation, SeeTreat, ...), deep learning-based sCT generation remains an emerging technique with limited clinical implementation (30). Therefore, the reproducibility and generalizability of the present findings will require confirmation through prospective clinical studies, including assessment of robustness, workflow integration, and regulatory considerations, before widespread clinical adoption can be considered.

The growing number of sCT generators developed using different deep learning methods presents a challenge too, as these networks are often trained on different datasets and anatomies, and evaluated using different metrics. This inconsistency makes it difficult to perform a standardized methodological comparison, which in turn hinders the ability to identify the optimal network design choices for clinical sCT tools. In this context, the SynthRAD2023 challenge (covering brain and pelvic patients), followed by SynthRAD2025 (covering head-and-neck, thorax, and abdomen), was designed to compare and benchmark synthetic CT generation methods using multi-center ground truth data (33–35). The SynthRAD2023 findings indicated no significant correlation between image similarity metrics and dosimetric accuracy, thereby highlighting the necessity of comprehensive dose evaluation when assessing the clinical viability of sCT in radiotherapy workflows (33). Furthermore, the absence of standardized criteria for assessing and reporting sCT quality has been recognized as a key factor impeding the clinical adoption of new methods (36). Developing a robust quality assurance process will be a future challenge to ensure the safe and reliable integration of deep learning technologies into clinical workflows (37).

## 5 Conclusion

This retrospective multi-center study has shown the potential of synthetic CT across various anatomical sites. This AI-based tool is clinically acceptable, allows for significantly faster image conversion, and may enhance the implementation of adaptive radiotherapy treatments.

## Data availability statement

The raw data supporting the conclusions of this article will be made available by the authors, without undue reservation.

## Ethics statement

Ethical approval was not required for the study involving humans in accordance with the local legislation and institutional requirements. Written informed consent to participate in this study was not required from the participants or the participants' legal guardians/next of kin in accordance with the national legislation and the institutional requirements.

## Author contributions

JP: Writing – original draft. LC: Conceptualization, Formal analysis, Writing – review & editing. SR: Conceptualization, Formal analysis, Writing – review & editing. OT: Conceptualization, Formal analysis, Writing – review & editing. DA: Writing – review & editing. NP: Writing – review & editing. PF: Conceptualization, Formal analysis, Validation, Writing – review & editing.

## Funding

The author(s) declared that financial support was not received for this work and/or its publication.

## Conflict of interest

NP: Chief Executive Officer; Therapanacea. Authors LC, SR and OT were employed by Therapanacea.

The remaining authors declared that this work was conducted in the absence of any commercial or financial relationships that could be construed as a potential conflict of interest.

The author DA declared that they were an editorial board member of Frontiers, at the time of submission. This had no impact on the peer review process and the final decision.

## Generative AI statement

The author(s) declared that generative AI was not used in the creation of this manuscript.

Any alternative text (alt text) provided alongside figures in this article has been generated by Frontiers with the support of artificial intelligence and reasonable efforts have been made to ensure accuracy, including review by the authors wherever possible. If you identify any issues, please contact us.

## Publisher's note

All claims expressed in this article are solely those of the authors and do not necessarily represent those of their affiliated

organizations, or those of the publisher, the editors and the reviewers. Any product that may be evaluated in this article, or claim that may be made by its manufacturer, is not guaranteed or endorsed by the publisher.

## Supplementary material

The Supplementary Material for this article can be found online at: <https://www.frontiersin.org/articles/10.3389/fonc.2026.1756153/full#supplementary-material>

## References

- Yan D. Adaptive radiotherapy: merging principle into clinical practice. *Semin Radiat Oncol.* (2010) 20:79–83. doi: 10.1016/j.semradonc.2009.11.001
- Glide-Hurst CK, Lee P, Yock AD, Olsen JR, Cao M, Siddiqui F, et al. Adaptive radiation therapy (ART) strategies and technical considerations: A state of the ART review from NRG oncology. *Int J Radiat Oncol Biol Phys.* (2021) 109:1054–75. doi: 10.1016/j.ijrobp.2020.10.021
- Olsen J, Green O, Kashani R. World's first application of MR-guidance for radiotherapy. *Mo Med.* (2015) 112:358–60.
- Acharya S, Fischer-Valuck BW, Kashani R, Parikh P, Yang D, Zhao T, et al. Online magnetic resonance image guided adaptive radiation therapy: first clinical applications. *Int J Radiat Oncol Biol Phys.* (2016) 94:394–403. doi: 10.1016/j.ijrobp.2015.10.015
- Archambault Y, Boylan C, Bullock D, Morgas T, Peltola J, Ruokokoski E, et al. Archambault: Making on-line adaptive radiotherapy. Google Scholar (2020) 8. Available online at: [https://scholar.google.com/scholar\\_lookup?journal=Med+Phys+Int+J&title=Making+on-line+adaptive+radiotherapy+possible+using+artificial+intelligence+and+machine+learning+for+efficient+daily+re-planning&author=Y+Archambault&author=C+Boylan&author=D+Bullock&volume=8&publication\\_year=2020&](https://scholar.google.com/scholar_lookup?journal=Med+Phys+Int+J&title=Making+on-line+adaptive+radiotherapy+possible+using+artificial+intelligence+and+machine+learning+for+efficient+daily+re-planning&author=Y+Archambault&author=C+Boylan&author=D+Bullock&volume=8&publication_year=2020&)
- Boda-Heggemann J, Lohr F, Wenz F, Flentje M, Guckenberger M. kV cone-beam CT-based IGRT: a clinical review. *Strahlenther Onkol.* (2011) 187:284–91. doi: 10.1007/s00066-011-2236-4
- Schulze R, Heil U, Gross D, Bruellmann DD, Dranischnikow E, Schwanecke U, et al. Artefacts in CBCT: a review. *Dentomaxillofac Radiol.* (2011) 40:265–73. doi: 10.1259/dmfr/30642039
- Giacometti V, Hounsfield AR, McGarry CK. A review of dose calculation approaches with cone beam CT in photon and proton therapy. *Phys Med.* (2020) 76:243–76. doi: 10.1016/j.ejmp.2020.06.017
- Barateau A, Céleste M, Lafond C, Henry O, Couespel S, Simon A, et al. Calcul de dose de radiothérapie à partir de tomographies coniques: état de l'art. *Cancer/Radiothérapie.* (2018) 22:85–100. doi: 10.1016/j.canrad.2017.07.050
- Veiga C, Janssens G, Teng CL, Baudier T, Hotoiu L, McClelland JR, et al. First clinical investigation of cone beam computed tomography and deformable registration for adaptive proton therapy for lung cancer. *Int J Radiat Oncol Biol Phys.* (2016) 95:549–59. doi: 10.1016/j.ijrobp.2016.01.055
- Simon A, Nassef M, Rigaud B, Cazoulat G, Castelli J, Lafond C, et al. Roles of Deformable Image Registration in adaptive RT: From contour propagation to dose monitoring. *Annu Int Conf IEEE Eng Med Biol Soc.* (2015) 2015:5215–8. doi: 10.1109/EMBC.2015.7319567
- Moteabbed M, Sharp GC, Wang Y, Trofimov A, Efstathiou JA, Lu HM. Validation of a deformable image registration technique for cone beam CT-based dose verification. *Med Phys.* (2015) 42:196–205. doi: 10.1118/1.4903292
- Sun M, Nagy T, Virshup G, Partain L, Oelhafen M, Star-Lack J. Correction for patient table-induced scattered radiation in cone-beam computed tomography (CBCT). *Med Phys.* (2011) 38:2058–73. doi: 10.1118/1.3557468
- Jin JY, Ren L, Liu Q, Kim J, Wen N, Guan H, et al. Combining scatter reduction and correction to improve image quality in cone-beam computed tomography (CBCT). *Med Phys.* (2010) 37:5634–44. doi: 10.1118/1.3497272
- Abe T, Tateoka K, Saito Y, Nakazawa T, Yano M, Nakata K, et al. Method for converting cone-beam CT values into hounsfield units for radiation treatment planning. *Int J Med Physics Clin Eng Radiat Oncol.* (2017) 6:361–75. doi: 10.4236/ijmpcero.2017.64032
- Spadea MF, Maspero M, Zaffino P, Seco J. Deep learning based synthetic-CT generation in radiotherapy and PET: A review. *Med Physics.* (2021) 48:6537–66. doi: 10.1002/mp.15150
- Rusanov B, Hassan GM, Reynolds M, Sabet M, Kendrick J, Rowshanfarzad P, et al. Deep learning methods for enhancing cone-beam CT image quality toward adaptive radiation therapy: A systematic review. *Med Physics.* (2022) 49:6019–54. doi: 10.1002/mp.15840
- van Elmpt W, Trier Taasti V, Redalen KR. Current and future developments of synthetic computed tomography generation for radiotherapy. *Phys Imaging Radiat Oncol.* (2023) 28:100521. doi: 10.1016/j.phro.2023.100521
- Sherwani MK, Gopalakrishnan S. A systematic literature review: deep learning techniques for synthetic medical image generation and their applications in radiotherapy. *Front Radiol.* (2024) 4:1385742. doi: 10.3389/fradi.2024.1385742
- Kida S, Nakamoto T, Nakano M, Nawa K, Haga A, Kotoku J, et al. Cone beam computed tomography image quality improvement using a deep convolutional neural network. *Cureus.* (2018) 10:e2548. doi: 10.7759/cureus.2548
- Xue X, Ding Y, Shi J, Hao X, Li X, Li D, et al. (CBCT) based synthetic CT generation using deep learning methods for dose calculation of nasopharyngeal carcinoma radiotherapy. *Technol Cancer Res Treat.* (2021) 20:15330338211062416. doi: 10.1177/15330338211062416
- Pang B, Si H, Liu M, Fu W, Zeng Y, Liu H, et al. Comparison and evaluation of different deep learning models of synthetic CT generation from CBCT for nasopharynx cancer adaptive proton therapy. *Med Phys.* (2023) 50:6920–30. doi: 10.1002/mp.16777
- Maspero M, Houweling AC, Savenije MHF, van Heijst TCF, Verhoeff JJC, Kotte ANTJ, et al. A single neural network for cone-beam computed tomography-based radiotherapy of head-and-neck, lung and breast cancer. *Phys Imaging Radiat Oncol.* (2020) 14:24–31. doi: 10.1016/j.phro.2020.04.002
- Liu X, Yang R, Xiong T, Yang X, Li W, Song L, et al. CBCT-to-CT synthesis for cervical cancer adaptive radiotherapy via U-net-based model hierarchically trained with hybrid dataset. *Cancers.* (2023) 15:5479. doi: 10.3390/cancers15225479
- Texier B, Hémon C, Lekieffre P, Collot E, Tahri S, Chourak H, et al. Computed tomography synthesis from magnetic resonance imaging using cycle Generative Adversarial Networks with multicenter learning. *Phys Imaging Radiat Oncol.* (2023) 28:100511. doi: 10.1016/j.phro.2023.100511
- Prunarett J, Gungör G, Gevaert T, Azria D, Valdenaire S, Balermppas P, et al. A multi-centric evaluation of self-learning GAN based pseudo-CT generation software for low field pelvic magnetic resonance imaging. *Front Oncol.* (2023) 13:1245054. doi: 10.3389/fonc.2023.1245054
- Biguri A, Dosanjh M, Hancock S, Soleimani M. *TIGRE: a MATLAB-GPU toolbox for CBCT image reconstruction.* IOPscience (2016) 2. doi: 10.1088/2057-1976/2/5/055010
- Wongtrakool P, Puttanawarut C, Changkaew P, Piasanthia S, Earwong P, Stansook N, et al. Synthetic CT generation from CBCT and MRI using StarGAN in the Pelvic Region. *Radiat Oncol.* (2025) 20:18. doi: 10.1186/s13014-025-02590-2
- de Hond YJM, Kerckhaert CEM, van Eijnatten MAJM, van Haaren PMA, Hurkmans CW, Tjissen RHN. Anatomical evaluation of deep-learning synthetic computed tomography images generated from male pelvis cone-beam computed tomography. *Phys Imaging Radiat Oncol.* (2023) 25:100416. doi: 10.1016/j.phro.2023.100416
- O'Hara CJ, Bird D, Al-Qaisieh B, Speight R. Assessment of CBCT-based synthetic CT generation accuracy for adaptive radiotherapy planning. *J Appl Clin Med Phys.* (2022) 23:e13737. doi: 10.1002/acm2.13737
- Xie K, Gao L, Xi Q, Zhang H, Zhang S, Zhang F, et al. New technique and application of truncated CBCT processing in adaptive radiotherapy for breast cancer. *Comput Methods Programs Biomedicine.* (2023) 231:107393. doi: 10.1016/j.cmpb.2023.107393
- Chen X, Qiu RLJ, Peng J, Shelton JW, Chang CW, Yang X, et al. CBCT-based synthetic CT image generation using a diffusion model for CBCT-guided lung radiotherapy. *Med Phys.* (2024) 51:8168–78. doi: 10.1002/mp.17328
- Huijben EMC, Terpstra ML, Galapon AJ, Pai S, Thummerer A, Koopmans P, et al. Generating synthetic computed tomography for radiotherapy: SynthRAD2023 challenge report. *Med Image Anal.* (2024) 97:103276. doi: 10.1016/j.media.2024.103276

34. Thummerer A, van der Bijl E, Galapon AJ, Verhoeff JJC, Langendijk JA, Both S, et al. SynthRAD2023 Grand Challenge dataset: Generating synthetic CT for radiotherapy. *Med Phys.* (2023) 50:4664–74. doi: 10.1002/mp.16529
35. Thummerer A, van der Bijl E, Galapon AJ, Kamp F, Savenije M, Muijs C, et al. SynthRAD2025 Grand Challenge dataset: Generating synthetic CTs for radiotherapy from head to abdomen. *Med Phys.* (2025) 52:e17981. doi: 10.1002/mp.17981
36. Kurz C, Buizza G, Landry G, Kamp F, Rabe M, Paganelli C, et al. Medical physics challenges in clinical MR-guided radiotherapy. *Radiat Oncol.* (2020) 15:93. doi: 10.1186/s13014-020-01524-4
37. Hurkmans C, Bibault JE, Brock KK, van Elmpt W, Feng M, David Fuller C, et al. A joint ESTRO and AAPM guideline for development, clinical validation and reporting of artificial intelligence models in radiation therapy. *Radiotherapy Oncol.* (2024) 197:110345. doi: 10.1016/j.radonc.2024.110345